

High Resolution Point Clouds from mmWave Radar

Akarsh Prabhakara
Carnegie Mellon University
aprabhak@andrew.cmu.edu

Tao Jin
Carnegie Mellon University
taojin@andrew.cmu.edu

Arnav Das
University of Washington
arnavmd2@uw.edu

Gantavya Bhatt
University of Washington
gbhatt2@uw.edu

Lilly Kumari
University of Washington
lkumari@uw.edu

Elahe Soltanaghei
University of Illinois
Urbana-Champaign
elahe@illinois.edu

Jeff Bilmes
University of Washington
blimes@uw.edu

Swarun Kumar
Carnegie Mellon University
swarun@cmu.edu

Anthony Rowe
Carnegie Mellon University
agr@ece.cmu.edu

Demo Video: <https://youtu.be/bBCllSwWGgQ>

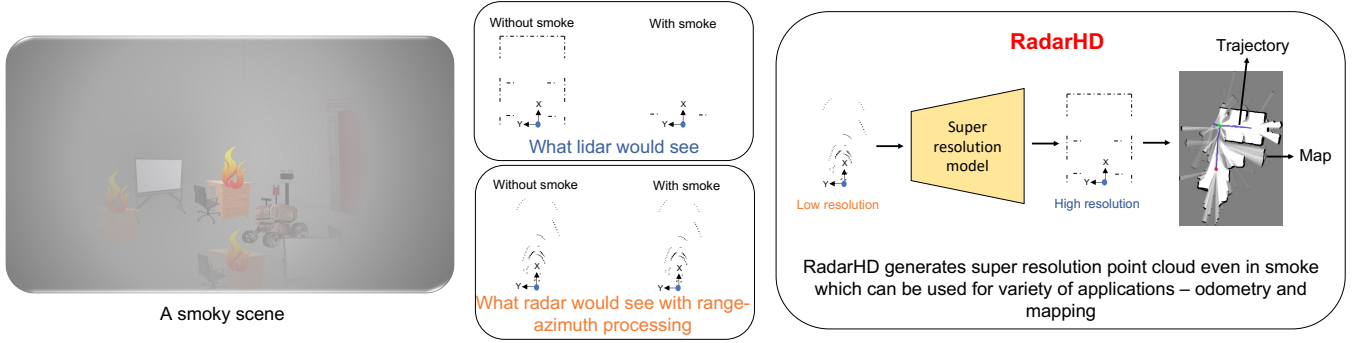


Figure 1: RadarHD enables perceiving environments with occlusions such as smoke, that are challenging for cameras and lidars, at a higher fidelity than that is possible with state-of-the-art single-chip radars.

ABSTRACT

This paper explores a machine learning approach for generating high resolution point clouds from a single-chip mmWave radar. Unlike lidar and vision-based systems, mmWave radar can operate in harsh environments and see through occlusions like smoke, fog, and dust. Unfortunately, current mmWave processing techniques offer poor spatial resolution compared to lidar point clouds. This paper presents RadarHD, an end-to-end neural network that constructs lidar-like point clouds from low resolution radar input. Enhancing radar images is challenging due to the presence of specular and spurious reflections. Radar data also doesn't map well to traditional image processing techniques due to the signal's sinc-like spreading pattern. We overcome these challenges by training RadarHD on a large volume of raw I/Q radar data paired with lidar point clouds across diverse indoor settings. Our experiments show the ability to generate rich point

clouds even in scenes unobserved during training and in the presence of heavy smoke occlusion. Further, RadarHD's point clouds are high-quality enough to work with existing lidar odometry and mapping workflows.

1 INTRODUCTION

Lidar is often considered the gold standard in terms of sensors used for mapping, localization, and collision avoidance applications. A key enabler is its ability to generate low-noise and high-density point clouds, which can be easily tracked from one position to the next. Despite being used ubiquitously, lidar, just like visible light cameras, fail when used in environments with occlusions – e.g. for firefighting in thick smoke (Fig. 1), automobiles in foggy weather, or phones kept inside pockets. These applications demand sensors that see past occlusions and sense the world in high fidelity.

Radars (the RF equivalent of lidars) show promise given the robustness of RF waves to occlusions [68]. However, due to the longer wavelengths of RF (even at mmWave frequencies), single-chip radars achieve an azimuth resolution that is two orders of magnitude (one-hundredth) that of a lidar. Therefore, a radar resolves point clouds at a much lower resolution than lidar, limiting them to coarse-grained collision avoidance type applications. Higher resolution applications often resort to large mechanical radars, adding bulk and cost. Our goal is to push the resolution limits of a lightweight and compact, single-chip radar, suitable for much more portable platforms (e.g. future small robots, drones, AR/VR headsets, and mobile phones). We specifically seek to exploit the enormous amounts of low-level RF data normally discarded by traditional mmWave processing pipelines to dramatically enhance resolution.

Current techniques to improve radar angular resolution include (1) synthetic aperture, which moves radars along specific trajectories precisely [25, 51, 53, 71, 77], and (2) multi-modality (camera or lidar) sensor fusion for better information on angular resolution [37, 39, 47]. However, neither of these are applicable for radars that can move arbitrarily, and as previously stated, occlusions cause auxiliary sensors like cameras and lidars to fail. Recent work has made initial steps toward using single-chip mmWave radars for odometry and mapping. These systems use low resolution radars alone to run range-doppler analysis [19, 20] and end-to-end neural networks [41, 42]. Both approaches directly solve for odometry (i.e. a single higher-level problem). Instead, we propose generating high resolution point cloud data directly from radar I/Q streams that can be used as a perceptual input for multiple types of processing pipelines. These point clouds enable a more general representation of the world that makes it easier to understand the output, debug errors and can be fed into traditional, existing point-cloud processing pipelines for odometry, mapping, and beyond.

We propose RadarHD, which is a custom-designed, end-to-end neural network that generates *lidar-like* point clouds from low resolution radar point clouds. Our approach is inspired by recent machine learning work on super resolution of images and videos [29, 70] where it is possible to collect a large body of high-fidelity ground-truth data (lidar) in support of boosting the performance of a lower-fidelity auxiliary sensor (mmWave). We opt for an end-to-end learning-based pipeline to generate point clouds from radar data, allowing for learning features ordinarily missed or thrown away by traditional signal processing pipelines. We show that our generated point clouds are excellent for scene capture, odometry, and mapping tasks, even in smoke-filled environments.

In designing RadarHD, we encountered two challenges. *First*, raw radar measurements are impacted by a various

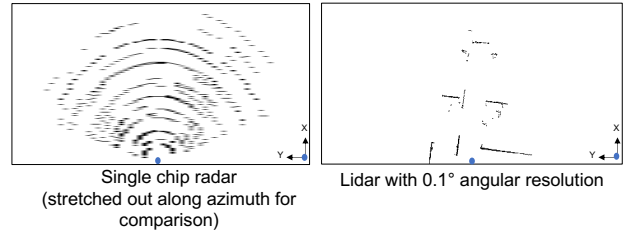


Figure 2: Single chip radar clearly has a much lower angular resolution than state-of-the-art lidar. Noticeably, radar also shows other spurious artifacts. ● marks the origin and both images show the same scene as perceived by each sensor in a 10x20m area.

spurious artifacts – sidelobes from strong reflectors that create sinc-like patterns across azimuth due to its poor azimuth resolution (see Fig. 2), specular reflections from certain objects, and other processing artifacts [7]. Eliminating these artifacts to recover true objects in the environment is crucial for constructing a dense and accurate point cloud. *Second*, radar images are coarse – meaning that they struggle with resolving sharp environmental features with high angular resolution. In other words, the data from a low resolution radar is quite different from low resolution camera images, where naive super resolution such as interpolation would give a sensible result.

RadarHD builds a custom neural network pipeline that uses raw radar captures to construct high resolution point clouds to address these concerns. RadarHD is trained using large data sets of radar-lidar pairs collected on identical scenes to help radar learn from lidar. An ideal super resolution model would first weed the spurious artifacts and uncover true reflections and, in the process, capture and reverse the *sinc-like* spreading and specular reflections to then perform super resolution. Key to RadarHD’s design is the decision to first convert sparse radar data to an *even sparser*, but *semantically accurate* representation of the true objects that eliminates spurious artifacts. RadarHD then upsamples this sparse representation to the desired dense point cloud resolution, guided by lidar point cloud representations of typical indoor spaces. To achieve this, RadarHD is inspired by the popular U-net architecture [57] from computer vision – used traditionally in image segmentation that also first obtains a semantic understanding and then upsamples to output segmentation masks. RadarHD builds on this architecture with key differences unique to the mmWave radar context (see Sec. 4). First, we transform the raw I/Q radar signals, which are quite different from traditional camera image inputs, into a form compatible with U-net models. Second, we adapt the U-net architecture to the super resolution problem and make key architectural choices to overcome radar artifacts while preserving desirable features. Finally, we carefully choose

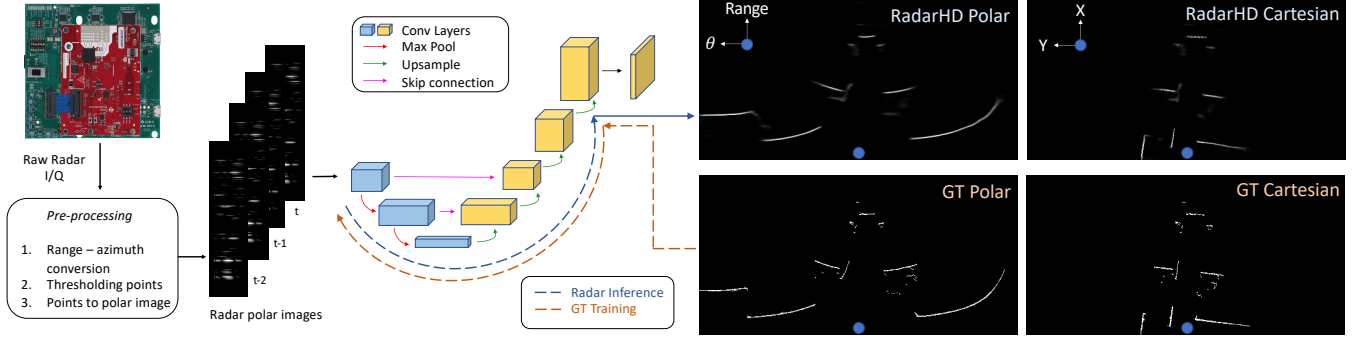


Figure 3: Overview: RadarHD performs super resolution of low resolution, pre-processed radar images using a custom designed neural network and generates lidar-like point clouds.

loss functions to ensure the sharp output of point clouds (e.g. sharp walls and corners as in Fig. 2).

Post-training and in the spirit of model interpretability, we use attribution analysis [34, 64, 65] to understand the learned model (Sec. 5). We employ input image attribution, assigning an importance score to different input pixels depending on their contribution to the super resolution image. We also perform layer attribution to understand what is learned by different network layers. This shows promise for elements of our architecture to be reused for other radar ML tasks.

To implement RadarHD, we collect a large repository (200k pairs) of raw I/Q radar data from TI AWR1843 mmWave radars paired with lidar point clouds across different buildings and floors for generalization. Non-synthetic, large-scale, raw I/Q radar data paired with lidar is not publicly available today. We believe that such a dataset enables designing data-driven algorithms while ensuring benchmarkable and reproducible results. RadarHD’s evaluation reveals: (1) Low point-cloud error (24 cm) versus the lidar ground-truth and 3.5 \times superior to traditional radar point-clouds; (2) Demonstration of two typical applications for point clouds - odometry and mapping, using Google Cartographer [28]; (3) A comprehensive characterization of system performance in smoky scenes and new, unseen environments.

Contributions: RadarHD makes three key contributions:

- A novel super resolution model for generating lidar-like point clouds from low resolution radar.
- A detailed understanding of the model layers to help design future models dealing with radar data.
- A large repository of raw radar I/Q and lidar pairs along with source code that will be released publicly.

2 RELATED WORK

Radar Super resolution: Increasing the resolution of Ground Penetrating Radar, near-infrared, or lidar has been much explored, either through image processing algorithms [16, 22,

52] or deep neural networks [17, 26, 36]. In radar, high resolution is usually achieved by using Synthetic-Aperture Radar (SAR) [43, 51, 53, 76, 77] or sensor fusion such as integrating radar and optical components [6, 21, 44, 63]. More recent techniques leverage deep learning to enhance 2D object detection [6, 25, 43, 44, 58] or estimate the 3D pose of humans [2, 79, 80]. However, these techniques typically work only at short ranges or use large antenna arrays. HawkEye [25] is the closest related work to RadarHD that uses a GAN architecture to recover high resolution shapes from raw low resolution mmWave heatmaps. However, it relies on mechanically scanning the mmWave radio on a 2D slider to perform SAR and emulate a 40x40 antenna array [24, 25] to collect data prior to feeding it into a GAN. While this solution is intended to image static objects, it is not designed for a radar that is static or moving in arbitrary trajectories. In contrast, RadarHD achieves high resolution point clouds using just a single-chip radar, without relying on SAR, in both static and uncontrolled mobile usecases.

Radar Odometry and Mapping: The robustness of radars in visually degraded environments has made radar odometry an attractive solution for estimating the relative motion of a platform (e.g. robots, drones, cars, etc). State-of-the-art radar odometry techniques [3–5, 11, 12, 54, 54, 55, 60–62, 69] mainly rely on scan matching, in which spatial features from the radar images are matched against previous scans or a pre-determined map. However, due to spurious reflections and artifacts in radar data, the accuracy of these methods significantly drop for low resolution radars. Follow-up research in this area relies on more complex modeling such as using velocity estimates from radar scans [8, 18, 20, 32, 33, 49], the fusion of radar and IMU data based on EKF [5, 19, 35, 59], or fusion of radar and RGB camera [45, 46, 48] to overcome radar limitations. Few other approaches involve end-to-end learning approaches for fusing radar and IMU to obtain odometry [42] or mapping [41] individually. RadarHD, on the other hand, seeks to create accurate point clouds which have rich

relative features for enabling odometry and rich structural features for enabling mapping.

Millimeter-wave Sensing: The mm-level wavelength and the wide bandwidth available at mmWave frequency range provide high ranging accuracy and sensitivity. Combined with the robustness of mmWave radios to different lighting and weather conditions have made mmWave a popular option for sensing purposes. Prior work adopts mmWave for indoor map construction [27, 40, 82], human activity sensing [38, 66, 72], object tracking [73, 75, 81], drone tracking [81], and indoor localization [50]. However, the angular resolution of mmWave sensing systems are quite limited compared to cameras and lidars due to fewer number of sensors (aka. antennas), resulting in lower spatial resolution for scene perception. RadarHD tackles this core problem by enabling lidar-like scene perception while leveraging the robustness of radars to occlusion or in visually degraded environments.

3 RADARHD OVERVIEW

Fig. 3 depicts RadarHD’s super resolution pipeline. RadarHD uses only radar as input to obtain lidar-like point clouds. RadarHD is a machine learning pipeline that trains on a repository of radar and lidar captures taken in diverse scenes. RadarHD addresses several key challenges (Sec. 1): an approach to feed raw I/Q inputs into RadarHD’s model, an architecture that eliminates spurious artifacts, and careful selection of loss functions that lead to a sharp quality output.

The rest of the paper is organized as follows. We first present RadarHD’s custom-designed neural network model in Sec. 4. Then in Sec. 5, we use input and layer attribution analysis to understand some of the layers that the model is learning. We finally present our data collection methodology and evaluation in Sec. 6 and 7.

4 RADARHD SYSTEM DESIGN

The core objective of RadarHD is to improve the resolution of the radar signals and make them *lidar-like*. At first blush, one may consider simply interpolating and upscaling the radar processed image (Fig. 2), much like super resolution solutions on camera images [67]. Unfortunately, super resolution imaging with radars is substantially different from cameras, because low resolution radar captures lack neighborhood similarity. Specifically, dominant reflectors in a radar image can lead to spurious artifacts that impact the entire image rather than its immediate neighborhood. As an example, consider Fig. 2, which shows *sinc-like* spreading across the azimuth axis at several range bins. This happens primarily when a strong reflector is present, and the spreading would start from the pixel corresponding to the true reflector position and create sidelobes along the azimuth axis at the same range bin. Tackling this azimuth coupling requires a global

view of the image, unlike camera images where a local neighborhood around a pixel gives reasonably good information to perform the interpolation. On top of this, owing to noise, radar images tend to have spurious “ghost points”, i.e. false detections of non-existent objects that need to be weeded out. If we had a sense of what is truly present in the real world, we could design a model to selectively ignore such false detections. In other words, a global understanding of the image is crucial so that false detections can be ignored when conditioned with the expected output. Hence, RadarHD goes beyond classical pixel-by-pixel approaches to explore end-to-end, data driven machine learning approaches.

ML Design Choice: Having motivated the need for end-to-end learning, we now motivate RadarHD’s specific choice of ML models. One may consider a simple CNN model that up-samples the input radar image into a more dense point cloud output. Convolution layers are quite natural in image data or inputs with strong spatial locality. However, a naïve implementation of a CNN will struggle with radar data. RadarHD must account for sinc-like spreading and ghost points, which effectively involves building an accurate model of which objects in the image are true, and which are mere artifacts. Therefore, as mentioned earlier, RadarHD builds on a U-net based architecture, inspired by computer vision techniques traditionally used on image data for segmentation and ports it to address a different super resolution problem given radar data. RadarHD’s design processes the radar data that contains sparse features to build an even sparser representation that omits erroneous artifacts. However, this sparser representation must preserve true objects in the scene and remain semantically accurate to allow for accurate reconstruction of point clouds of these objects.

Design Challenges: The rest of this section describes several key system design challenges in designing RadarHD’s ML architecture. (1) First, we consider the problem of effectively representing, pre-processing, and inputting I/Q data to the model. (2) Second, we present a careful design of the U-net itself to allow for the elimination of spurious artifacts while preserving data from true objects in the scene. (3) Finally, we design loss functions to ensure that features such as sharp lines in the expected output (see Fig. 3) are preserved.

4.1 Radar Data Representation

We first consider the problem of feeding in an accurate form of mmWave radar signals as input to the ML architecture. To do so, we first briefly describe our radar platform’s capabilities and typical output.

Radar Platform: The specific choice of mmWave radar we consider is single-chip and uses Frequency Modulated Continuous Wave (FMCW) [30]. This platform provides raw I/Q data streams that can undergo further processing as needed.

A typical FMCW radar processing pipeline [31] involves a spatial Fourier transform that outputs a 2D heatmap that shows the intensity of the reflected radar signal across the range and azimuth angle. A traditional radar system applies a certain threshold on this heatmap to identify strong reflectors to provide a representation akin to a “point cloud”. The choice of threshold is application-dependent. For instance, aircraft radars select high thresholds to detect airplanes while most other artifacts in the open skies are not as dominant.

Choice of Input Representation: At this point, we have a choice – do we feed in raw I/Q inputs directly into the ML model, or should we send processed point cloud data. On the one hand, sending in raw I/Q inputs requires the model to understand and learn phase information and to learn some fairly obvious initial steps (e.g. a Fourier Transform). On the other hand, sending in a thresholded heatmap may filter out important information that values below the threshold carry, e.g. feeble objects masked by sinc lobes from stronger reflections.

RadarHD instead takes an approach that takes a middle path between these two extremes. Specifically, RadarHD applies a very low threshold to the heatmap so that it preserves dominant reflectors, feeble ones and many artifacts. Our objective is to retain a significant portion of the heatmap, including the most feeble reflectors while leaving it to the ML model to identify and filter out spurious artifacts. At the end of this process, we have thresholded points on the heatmap with range, azimuth, and intensity which can be arranged into an image with range (0-10 m) along rows and azimuth (-90° to 90°) along columns, as shown in see Fig. 3. Note that radar images (64×256) are narrower than lidar (512×256) because of the poorer azimuth resolution.

Polar vs Cartesian Coordinates: We note that the thresholded image above is still in polar coordinates, i.e. along the range-azimuth axes. One can convert this polar representation to a Cartesian format for easy understanding. However, to provide an input image to the neural network, we need to decide between a polar and Cartesian representation. At first blush, given that the output we desire for a point cloud is Cartesian (and it is quite easy to interpret), one may consider the Cartesian representation as the natural choice.

Studying a candidate Cartesian representation, e.g. in Fig. 2, leads us to a different conclusion. We specifically call attention to the radial distribution of points because radar inherently measures radially. Further, *sinc-like* side lobes arising from a strong reflector also spread azimuthally. To capture these radial and azimuthal variations, one would need radial/azimuthal processing. However, the primary learning element in convolutional layers in machine learning is a filter that performs a 2D correlation across the height and width of the input image. To leverage this to our advantage,

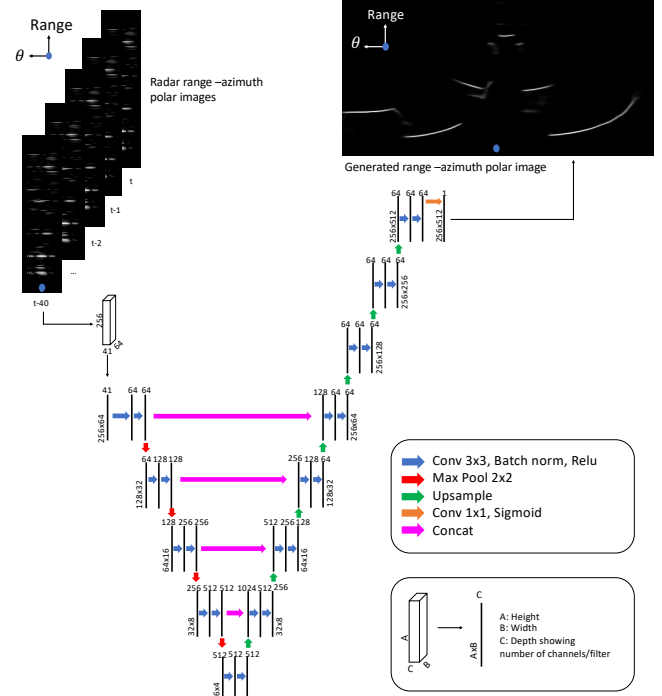


Figure 4: Assymetric U-net Network architecture: RadarHD adapts an encoder-decoder architecture for the radar super resolution task. Colored arrows show different ML operations. Black solid lines represent the 3D input and output of these operations.

we choose a polar format so that the filters then naturally traverse along the range and azimuth when they go across height and width, respectively. We also maintain consistency between input and output formats so that the locality of pixels that map from input to output is similar.

4.2 Neural network architecture

In designing our network, the two key objectives are to first obtain a global semantic understanding from the radar image and then use the understanding to upsample and create a high resolution *lidar-like* image. This leads us to encoder-decoder architectures where the encoder (marked blue in Fig. 3) captures the semantic understanding, and the decoder (marked yellow in Fig. 3) performs the upsampling. Ideally, our encoder would capture pixel, neighborhood, and global understanding at different resolutions. Traditionally, this is done using a cascade of convolutional layers and “max pool” or downsampling operations wherein convolutional layers capture the spatial variation for each downsampled resolution. The decoder uses this semantic understanding from encoder and it is generally chosen to be symmetric to the encoder but using upsampling operations instead.

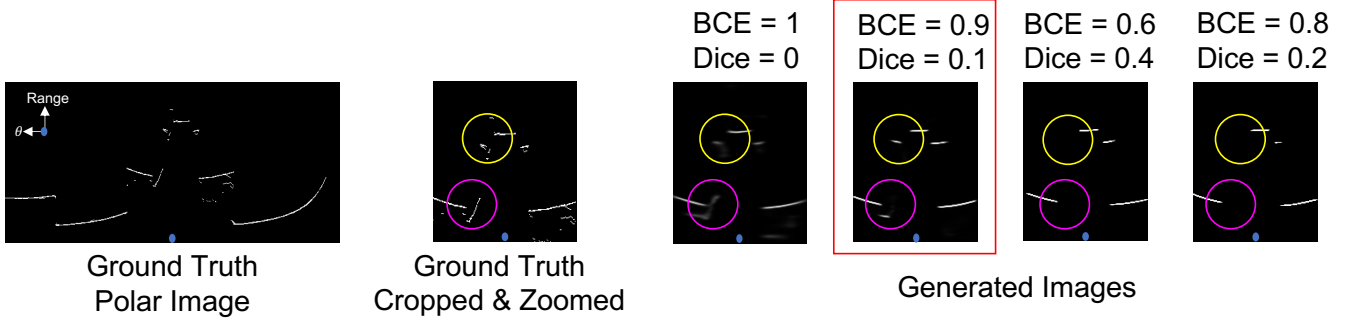


Figure 5: Qualitative Ablation Study: Dice Loss helps in sharpening lines, but is very aggressive and starts missing out features shown in colored circles. RadarHD chooses a balance between sharpness and accuracy.

Drawing inspiration from computer vision, where encoder-decoder architectures have been used for many tasks such as image segmentation, we choose our base architecture to be the popular U-net architecture [57] (see Fig. 4). U-net uses a cascade of convolutional layers, batch norm, and ReLU activations at each "resolution level". In the encoder, U-net uses max pool operations to downsample and move to lower resolutions, and in the decoder, it uses upsampling to move to higher resolutions. From Fig. 4, we can also clearly see that as we move to lower resolutions, the height and width of convolution output decreases (implying capturing more global understanding), and the number of filters increases (to capture richer global understanding). RadarHD’s design however has several salient differences from traditional U-nets in computer vision stemming from unique challenges of the radar super resolution context.

U-net Asymmetry due to Super Resolution: While the base U-net is generally a symmetric network, our super resolution problem is fundamentally asymmetric. That is, the width of input images is smaller than the output image width. To tackle this, we adapt the base U-net to an *asymmetric U-net* by adding more upsampling and convolutional layers to the decoder to obtain the desired resolution (Fig. 4).

Mitigating Specularity: While the input data representation allows the U-net to capture the radial and azimuth variations in radar image data, one key challenge that remains is the specularity of some radar reflections. Specularity impacts reflected signal power with changes to the relative orientation between the object and the radar. In other words, points on objects that reflect and pass the threshold when viewed from one location disappear when viewed from other locations. One way to deal with this is to view the scene from multiple viewpoints. Indeed, our envisioned application scenarios involve the radar being carried around by a robot/human. We can naturally obtain multiple viewpoints by looking at the time series of radar image frames. The need for multiple viewpoints is further exacerbated when

we empirically observed the lack of persistence in the inferred images when using just one radar image as the output. That is, when the generated images are viewed as a video, objects would appear and disappear. Thus, it is important to consider using these multi-viewpoint images to tackle specularity and establish a notion of persistence.

Naively one could use single frame inference and classical filtering to ensure that objects do not appear and disappear. However, we explored an end-to-end approach that incorporates past radar frames in the network while performing super resolution on the current frame to see if it improved inferences. We observe that in the first convolutional layer, a new filter is learned for different channels of the input image (so far assumed to be 1 as we just have radar intensity at each pixel). This implies that the network is first capable of learning structural patterns across different input image channels individually and later in subsequent layers combine all the learned patterns. If we were to embed the multi-view radar images as input channels, we not only ensure understanding of each radar image but also allow the network to model persistence when combining the learned understanding. Therefore, although the base U-net was designed for a single input image, our idea is to exploit the option of a variable number of input image channels and stack past radar frames along the channel axis before giving as input. In Sec. 7.1, we quantitatively show the benefits of including past frames in input.

4.3 Neural network training methodology

Training our network involves careful selection of loss functions to obtain sharp lidar-like images which include thin lines of white pixels amidst a neighborhood of black pixels. We use a combination of various loss functions for achieving different objectives.

Pixel wise loss: To compare two images, one ground-truth label and one output from the network, we first consider the most standard loss function – pixel wise loss. While the input image contains intensity information obtained from

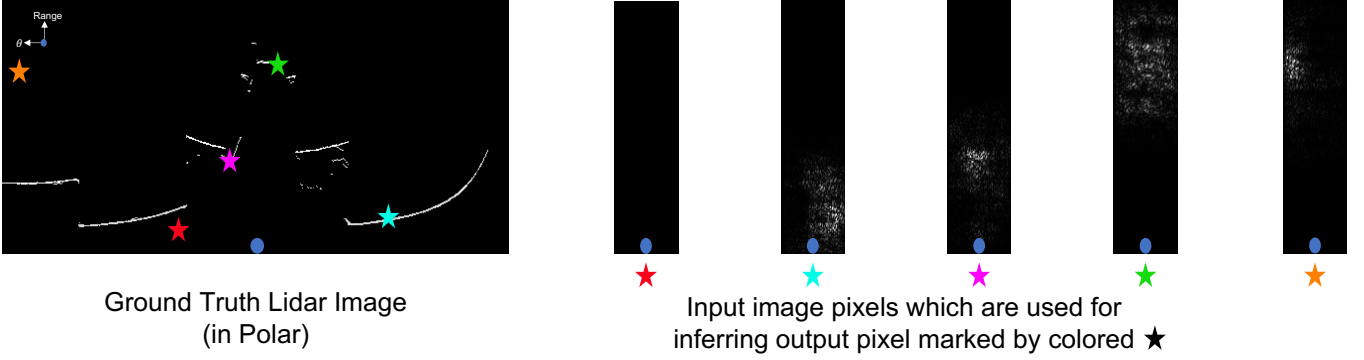


Figure 6: Input attribution map: This figure shows which input pixels matter to the network for generating each output pixel. It can be seen that: (1) in pixels where points are absent in the ground truth (★), no input pixel is used, (2) in pixels where points are present in the ground truth (★ ★ ★), input pixels in the neighborhood of pixel of interest are used by the network and (3) sometimes even though pixels are absent in the ground truth (★), input pixels in the neighborhood are used to ensure that the network doesn't output a false point.

pre-processing, our ground truth labels are binary lidar images indicating whether an object is present at a pixel or not. We compare this binary image against the final sigmoid layer output from the network. The sigmoid layers keep the value of inferred pixels between 0 and 1. We use Binary Cross-Entropy (BCE) to compare each pixel and then take the mean over all pixels. The objective of a pixel wise loss is to force each pixel to match that of the expected output. From Fig. 5, we see that pixel wise loss achieves a reasonable approximation of expected output, but the lines and boundaries are not quite as sharp as the ground truth.

Dice loss: To promote crisp and sharp lines in the output image, we draw inspiration from losses used in computer vision tasks like boundary detection [14]. Dice loss [1] is one such loss function. For each pixel in ground-truth g_i and network output o_i , Dice loss for N pixels is defined as:

$$D = 1 - \frac{2 \sum_{i=1}^N o_i g_i}{\sum_{i=1}^N o_i^2 + \sum_{i=1}^N g_i^2}$$

Here, the numerator finds the loss pixel wise and is maximized when both o and g are identical. The denominator, however, keeps a global view of total number of points that are 1. When o and g are identical, the ratio is 1 and loss is 0. So, the loss promotes maximizing the intersection between o and g and penalizes the union of o and g . This forces the network to output 1 exactly where the ground truth is 1, while remaining 0 where the ground truth is 0. This enables a sharper and crisper prediction than pixel wise cross entropy. Fig. 5 qualitatively shows that adding Dice loss improves the sharpness of lines in the network's output.

5 MODEL INTERPRETABILITY

Our network outputs a general-purpose high resolution image that can be used for odometry, mapping, and other applications. One of the key benefits of such a general-purpose representation rather than end-to-end odometry or mapping ML pipelines is the ability to debug when something goes wrong. For example, if the high resolution image is not accurate for a particular environment, we expect the odometry and mapping to have errors. However, discovering what went wrong merely using odometry output from the network can be challenging in an end-to-end odometry pipeline.

We now focus on the interpretability of our model. In machine learning literature, attribution techniques have been used to understand what different network layers learn. For example, convolutional networks for image classification have been shown to capture low-level information in the earlier layers and higher-level information in deeper layers [78]. Beyond this, attribution techniques have been used for understanding the influence of input, data distribution, and robustness to noise [23, 65]. For our model, we specifically look at the influence of input and layer attributions.

5.1 Input Attribution

Input attribution assigns an importance score to different features in the input, in our case, different pixels of the input radar image. Of the available input attribution techniques, we use Saliency [34, 65]. Intuitively, for a simple linear model ($w^T x + b$), the magnitude of weights w decide which elements of x are important. Saliency extends this to complicated non-linear models, such as our network. Given an input image, a trained model, and an output pixel of interest, Saliency computes the importance score for each individual input

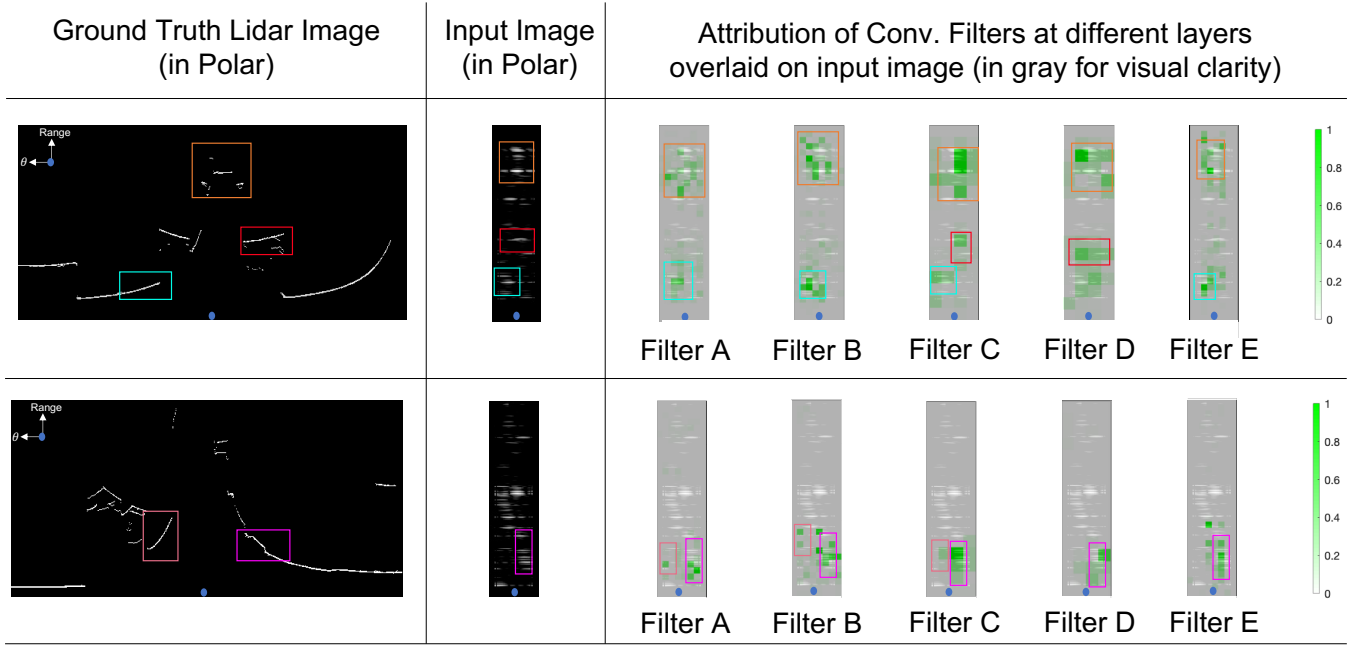


Figure 7: Layer Attribution: This figure shows the layer attributions marked in green at 5 filters at the bottom two resolution levels of RadarHD. The green values show which input pixels matter in predicting white pixels in the output. Clearly, we can see major objects in the environment (shown in colored boxes on the left) triggering the filter attributions on the right. Thus, our model declutters and captures the semantic understanding of the scene.

pixel. In other words, the Saliency score represents how much an input pixel matters in generating the output pixel.

Fig. 6 shows the Saliency scores of 5 different output pixels of interest marked with colored \star . The Saliency score is of the same shape as the input as it is computed for each input pixel. We highlight a few key takeaways of this analysis:

- \star : For inferring pixels which are not occupied in the output ground truth, the model learns to ignore all input pixels and not use any information. Intuitively, we expect the model only to use input pixels when the output pixel of interest is occupied. This result matches our intuition.
- $\star \star \star$: For inferring pixels which are occupied in the ground truth, we see that the input pixels used are in the same local neighborhood as the output pixel. For $\star \star$ and \star , we accordingly see input pixels in the right bottom corner, center, and top center respectively to be marked as useful. We also note that the input pixels used tend to occupy local 2D regions. This could refer to the process of the model learning *sinc-like* patterns and using all the sidelobes to un-distort the input image.
- \star : Sometimes even for inferring pixels which are not occupied, we see that certain input pixels in the neighborhood are used. This implies that the structure of the scene in the input image (unlike images used in training) required using all nearby pixels to avoid showing a false output.

Overall, we find that input attribution shows us that the locality of input pixels used are indeed pixels relevant to the output.

5.2 Layer Attribution

Layer attribution seeks to understand what is learned by each layer in the model. Recall that our entire network architecture was designed to ensure that the encoder captures the radar artifacts and achieves a semantic understanding while the decoder uses this understanding to perform the upsampling. Here, we focus on obtaining the semantic knowledge of the scene that the encoder captures from noisy input.

Our objective is to study the activations of different convolutional filters, especially in the encoder. We use Layer Conductances [15, 34, 64], a technique for layer attribution. The output *attribution* is a 0 to 1 image, one for each filter, with dimensions being the height and width of the filter. Values closer to 1 mark filter weights which are important. As we move lower down the encoder, the filter sizes become smaller and smaller. For sizes smaller than the input dimensions, we upsample the attribution and overlay it on the input image, as shown in Fig. 7. Note that attributions are slightly different from activations in the sense that they capture the activations that matter in inferring a particular region of output pixels. In our case, we use it to look for

patterns across filters for generating the white pixels in the output image. We would like to highlight the following key takeaways after studying all 1472 (64+128+256+512+512) terminal convolution filters at each of the 5 "resolution levels" in the encoder (see Fig. 7).

- We find that the attributions across different filters are mostly sparse. Most filters contain mostly 0s except for a few values close to 1. This is characteristic of convolutional layer-based encoder networks [78]. For typical input data as shown in Fig. 7, we see 10, 26, 68, 8, and 4 filters at each resolution level, respectively, to contain non-zero attribution. This shows that few filters contribute to generating the white pixels. We also observe that the number of total activations is denser than attributions. This shows that apart from the few filters mentioned above that contribute to the white pixels, many other filters do get activated and contribute to the black pixels.
- Next, we look at the non-zero filter attributions, especially at the bottom-most two resolution levels, which typically capture high-level information [13]. Five filter attributions from the bottom layers are overlaid on the input image in Fig. 7. Our first point to note is that the attributions are significantly less noisy in contrast to the input image. This shows that the encoder does declutter the scene and eliminate the artifacts. In comparison to the ground truth, all important and true reflections in the scene are identified in their correct positions across the five attributions. This tells us that the semantic understanding as interpreted from these attributions accurately represents the real world devoid of radar artifacts. Also, most importantly, because this encoder captures the semantic information, we believe the encoder design can be reused for several other radar tasks beyond super resolution, such as object detection and classification, to name a few.

6 IMPLEMENTATION

System Hardware: RadarHD was implemented using TI mmWave radar AWR1843, a state-of-the-art single-chip radar with a theoretical range resolution of 3.75 cm and azimuth resolution of 15° . RadarHD’s objective is to improve this azimuth resolution. We use the AWR1843 together with a DCA1000EVM (data capture board) to store raw I/Q samples. The radar is configured to operate up to a 20-meter radius at 20Hz frame rate. Although the radar supports elevation angle of arrival, we restrict ourselves to range-azimuth only, instead of full-fledged 3D configuration, primarily because its elevation resolution is significantly poorer than azimuth (3D should be explored as future work).

Testbed and Data Collection: Our testbed consists of the aforementioned radar and other time-synchronized sensors like lidar for ground truth and a camera for debugging. Our

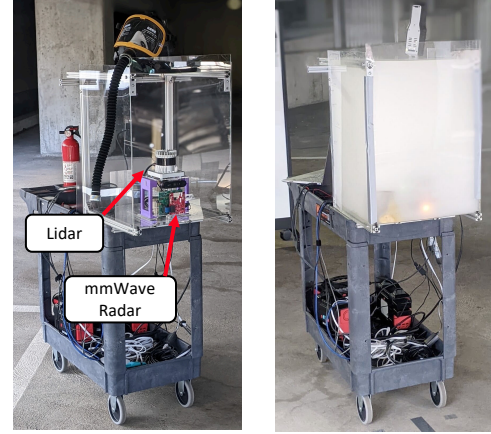


Figure 8: RadarHD implementation setup with a mmWave radar, lidar and smoke chamber.

testbed is mounted on a cart, as shown in Fig. 8, without the smoke chamber for all collection environments without occlusion such as smoke. The cart is pushed by humans at speeds ranging between 0-1 m/s, typical of robots and humans. We collect our data across several rooms in different buildings, including office spaces with cubicles, lobby areas, long corridors, etc., spanning a total area of $5147 m^2$. Our entire data repository consists of about 200k radar I/Q - lidar pairs, which we believe will be extremely useful to the research community.

Ground Truth: We use Ouster OS 0 - 64 beam mechanical scanning lidar for our ground truth. This lidar provides a 360-degree azimuth field of view. However, since the radar is only front-facing, we only use the forward-facing lidar points for super resolution. The lidar is configured to obtain 0.35° azimuth resolution also at 20Hz. Because we are only using azimuth angle of arrival on radar, we restrict the lidar’s elevation field of view to be within $\pm 30^\circ$. Additionally, this lidar operates at an 865 nm near-infrared spectrum, which would be susceptible to particulate matter of comparable size.

Baselines: We use Constant False Alarm Rate (CFAR) based thresholding with different thresholds as our baselines. Today, without super resolution, CFAR is the most widely used feature extractor for collecting radar point clouds from single-chip radars. Setting lower thresholds leads to denser point clouds but with no visible structural correspondence with the real world (Fig. 2). Specifically, we implement Cell-Averaging CFAR [56] on our collected raw I/Q data. We use this as a baseline for point cloud comparison, odometry, and mapping applications.

Train and Test Data: We train our system in a large office space that includes furniture, electronics, walls, conference

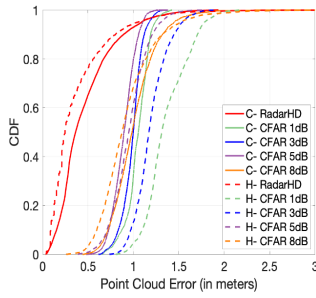


Figure 9: RadarHD point cloud error.
C- Chamfer H- Mod. Hausdorff

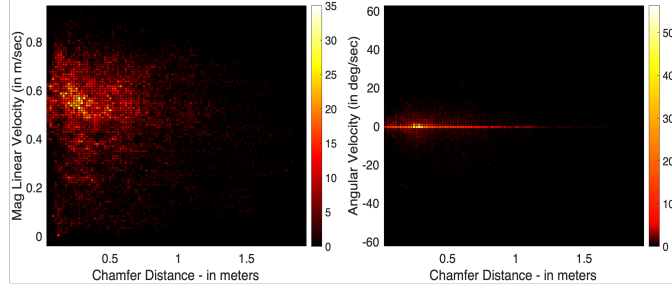


Figure 10: Histogram of RadarHD error wrt mobility.

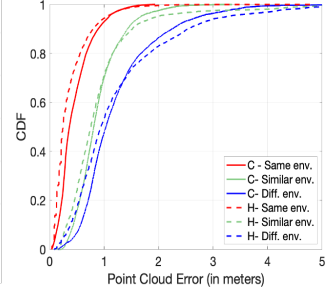


Figure 11: RadarHD error in similar and different environments.

Effectiveness of past frames		Effectiveness of Dice Loss			
No. past frames	MAE	BCE weight	Dice weight	BCE Loss	Dice Loss
0	2978.7	1.0	0.0	0.037	0.79
2	1189.5	0.9	0.1	0.048	0.72
20	401.15	0.8	0.2	0.057	0.73
30	320.25	0.6	0.4	0.068	0.73
40	277.44	0.2	0.8	0.081	0.70

Table 1: Ablation study of our neural network design decisions. MAE - Mean Absolute Error

rooms, and cubicles, with a total area of 839 m^2 . All of our tests are performed on unseen data in (1) *same environment* with different trajectories collected across different days, (2) *similar environment* in a different office space with different cubicle structures, and (3) *different environment*, which is totally new and includes building lobbies and outdoor environments. We also safely tested our system’s sensitivity to smoke using smoke pellets placed inside a smoke chamber to simulate dense smoke conditions (Fig. 8). Across all our data we use a total of 28 trajectories for training (561 meters long with 22784 image pairs in total) and 39 diverse trajectories for testing (714 meters long with 36779 image pairs in total) to allow for testing robustly.

7 RESULTS

7.1 Ablation study

We first evaluate our neural network design choices using a quantitative ablation study. Of all design choices, here we show the (1) effectiveness of using past radar frames in ensuring a notion of persistence and tackling specularity, and (2) effectiveness of Dice loss in creating sharp images.

Past frames: We train models each with different number of past radar frames as input - varying from 0 to 40 timesteps (2 secs). We perform inference on a validation set in a static

environment. This allows us to check whether the inference as a time series is stable. We compare the mean absolute error in frame difference of the inferred frames. The lower the error, the more stable the inference is over time. We see $2.5\times$ improvement just by choosing 2 past frames (Table. 1) versus no past frames. Our final system chooses 40 frames (2 secs) as our past frame window as we observed diminishing improvement beyond 40.

Dice Loss: As mentioned in Sec. 4.3, Dice loss is important in ensuring the sharpness of images. However, Dice loss is very aggressive and misses on important point clouds if used without a pixel wise loss like binary cross entropy (BCE). We train with different weights for BCE and Dice loss and compare their performance on a validation set in Table. 1. Dice loss instantly improves performance upon adding even a 0.1 Dice loss weight. Dice loss improves with more and more weight but, as a trade-off, worsens BCE loss. So, we need to find an operating point that balances BCE and dice-loss. We choose $\text{BCE}=0.9$ and $\text{Dice}=0.1$ as they return the best point cloud both quantitatively and qualitatively.

7.2 Point cloud Comparison

Method: Having trained on rich office space environment, we first run through our network on all the diverse test samples. Up to this point, we have been visualizing our generated output (Fig. 5) as an 8-bit polar image. To convert to a point cloud for comparison with lidar ground truth, we first convert to Cartesian and threshold the image to obtain a list of points with their (x,y) location. We then compare point cloud error using two popularly used point cloud similarity metrics: (1) Chamfer distance [9]: finds the nearest neighbor for each point in one point cloud to the other, and takes the mean of all these distances to get an error for each point cloud pair. (2) Modified Hausdorff Distance [10]: which also finds the nearest neighbors and obtains the median of the respective neighbor distances.

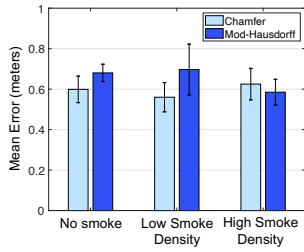


Figure 12: RadarHD is unaffected in smoke

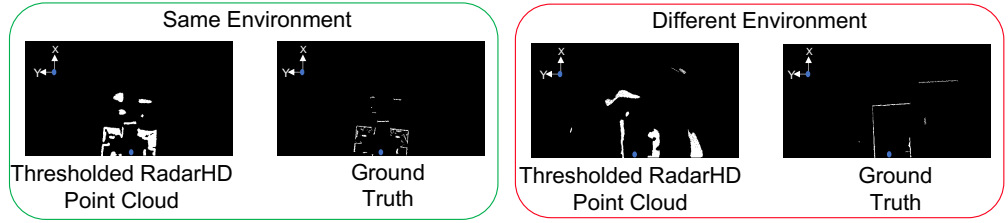


Figure 13: RadarHD thresholds generated images to compare with lidar. Note that although the generated images are sharp, to consider all points, we threshold the image to get a point cloud. ● marks the origin and all images show a 10x20m area.

Comparison to baseline: Here, we show our performance in the floor-wide office environment on 19 different trajectories against different CFAR thresholds. This includes 18k radar-lidar point cloud pairs, each over a 10x20 meter area.

As seen in Fig. 9, we obtain a 0.24 m modified-Hausdorff median error and 0.36 m Chamfer median error. CFAR, on the other hand, varies depending on the threshold. A low threshold like 1dB threshold creates point cloud 5x denser than lidar, while a high threshold like 8dB would just have 10% of the size of lidar. Despite varying density levels across these extremes, none of them have any structural similarity to the ground truth lidar point cloud. For example, a 5dB threshold would generate point cloud as seen in Fig. 2. So from 1dB to 8dB, as the threshold increases and density decreases, both point cloud error metric CDFs shift to the left. However, because the highest threshold generates a very sparse point cloud and does not resemble ground truth, the CDFs do not shift any more to the left with an increase in the threshold. In fact, beyond 8dB, the point cloud size was less than 1% the size of lidar. Our generated point cloud not only improves upon CFAR by 3.5x (mod-Hausdorff) and 2.7x (Chamfer), but is also structurally more similar to the ground truth as seen in Fig. 13, unlike CFAR as seen in Fig. 2.

Mobility: We next analyze the sensitivity of our system with respect to mobility on the same 19 trajectories with 18k point cloud pairs. Note that our sensor setup is mounted on a cart allowing for motion in 2D, which can be captured with linear velocity and angular velocity about the axis perpendicular to the floor. We obtain the true instantaneous velocities from the ground truth lidar by running it through SLAM [28].

Fig. 10 shows the distribution of Chamfer distance with respect to linear velocities. We see that as the speed changes from 0 to 0.9 m/s, the Chamfer distance remains concentrated between 0.2 m and 0.4 m, with the mode of the histogram showing 0.27 m at 0.56 m/s. This shows that our system can work well for typical robotic velocities in disaster recovery or firefighting applications. Next, we also point out that across different angular velocities, the Chamfer distance is

concentrated between 0.2 and 0.4 m, showing the robustness of point clouds generated during turns in the trajectory.

Generalization: We compare the performance of point cloud generation along 19 diverse trajectories against point clouds obtained along trajectories in *similar* and *different* environments without re-training. We use 7.5k point cloud pairs, each for *similar* and *different* environments.

Fig. 11 shows the change in performance in new environments. We see a median error of 0.75 m (mod-Hausdorff) and 0.8 m (Chamfer) for *similar* environments and 0.94 m (mod-Hausdorff) and 1.03 m (Chamfer) for *different* environments. This tells us that these point clouds generated are not quite as accurate as when trained in the same environment. At first glance, we observe that these medians are similar to the medians for some CFAR CDFs in Fig. 9. However, we would like to point out three important reasons why RadarHD’s point clouds are superior. First, the CFAR CDFs start on the x-axis at 0.4 m; in contrast, even for *similar* and *different* environments, we see that the CDFs start at 0.08 m. This shows that there is a significant fraction of the point clouds that is accurately inferred by our system. Second, because both Chamfer distance and modified Hausdorff distance have a nearest neighbor point association, structural similarity is not entirely captured [74]. However, we can qualitatively see from Fig. 13 that our system does successfully generate meaningful points. Third, to quantitatively show the impact of improved accuracy, we compare RadarHD against CFAR in two key applications - odometry and mapping in Sec. 7.3.

Smoke: To study the impact of smoke, we build a smoke chamber as in Fig. 8 and drop smoke pellets in it to create dense smoke. We remain static and capture the same scene without smoke and varying levels of smoke. Because our air particle counter saturated quickly in the smoke, we use onboard camera to judge the intensity of smoke.

We notice that even with 1 smoke pellet, which generates 500 cubic feet/min, our lidar does not receive any points. However, the sampled radar signals in smoke are almost identical to that without smoke even for the densest smoke

ATE (meter)	CFAR		RadarHD		
	3dB	8dB	Same env.	Similar env.	Diff env.
Mean	5.02	3.21	1.03	1.30	1.28
RMSE	5.74	3.98	1.35	1.52	1.44
Median	5.70	2.42	0.80	1.22	1.21
Std	2.79	2.35	0.87	0.80	0.68

Table 2: Odometry: Absolute Trajectory Error

RPE Rot. (in °)	CFAR		RadarHD		
	3dB	8dB	Same env.	Similar env.	Diff env.
Mean	26.95	12.51	2.12	3.62	2.74
RMSE	42.59	29.10	3.58	6.31	4.64
Median	12.61	4.25	1.30	2.22	1.60
Std	32.98	26.26	2.88	5.18	3.74

Table 4: Odometry: Relative Pose Error - Rotation

Map Error (meter)	RadarHD		
	Same env.	Similar env.	Diff env.
Mean	2.03	2.61	3.17
RMSE	2.70	3.58	3.87
Median	1.32	0.91	2.02
Std	1.78	2.44	2.22

Table 5: Mapping Error

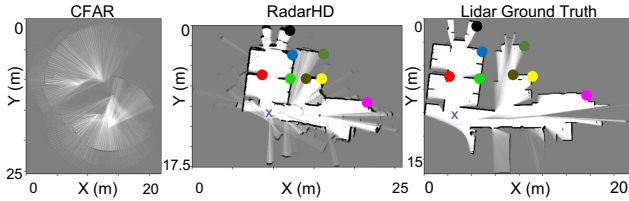


Figure 15: Mapping Examples. Colored points show physically similar *keypoints*. *x* is the start of trajectory.

we could create using 4 smoke pellets. As the radar signal remains the same, Fig. 12 shows that RadarHD’s performance does not degrade, up to the densities we could create.

7.3 Odometry Comparison

Using the point clouds generated, one application that RadarHD will enable is accurate odometry in scenarios where lidars fail. We evaluate this by feeding in our point clouds, without adding any other sensor (e.g IMU), into existing lidar SLAM frameworks such as Google Cartographer [28]. We obtain

RPE Trans. (meter)	CFAR		RadarHD		
	3dB	8dB	Same env.	Similar env.	Diff env.
Mean	2.50	0.10	0.07	0.09	0.08
RMSE	2.62	0.15	0.10	0.12	0.11
Median	2.54	0.07	0.05	0.07	0.05
Std	0.79	0.12	0.07	0.08	0.08

Table 3: Odometry: Relative Pose Error - Translation

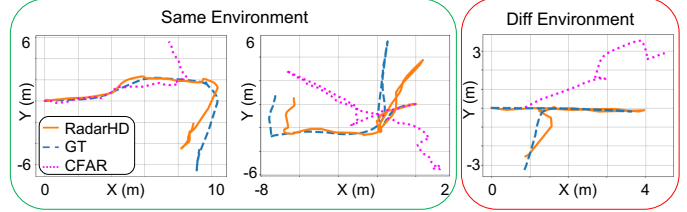


Figure 14: Odometry Examples

the 3-DoF pose in 2D - translation (*x,y*) and rotation - from Cartographer. We then evaluate against lidar and benchmark CFAR point clouds using widely adopted metrics such as Absolute Trajectory Error (ATE) and Relative Pose Error (RPE). Table. 2 demonstrates the long-term trajectory accuracy, whereas Table. 3 and Table. 4 shows the short-term odometry drift for translation and rotations, respectively.

In all cases, including *different* environments, the odometry accuracy of RadarHD outperforms that of CFAR regardless of threshold. Qualitatively, one can clearly see the difference between RadarHD odometry and CFAR odometry in Fig. 14. RadarHD achieves performance comparable to radar+IMU pipelines dedicated for odometry in past work [42]. When comparing our results to other multi-modal sensor fusion odometry systems such as VINET/DINET [42], RadarHD still achieves better performance.

7.4 Mapping Comparison

We next evaluate the generated point cloud for mapping task. We benchmark the mapping performance of RadarHD by identifying *keypoints* that point to the same physical feature in the real world, such as corners of a room, and then calculate the Euclidean distance error of corresponding *keypoints* between RadarHD and ground truth. Fig. 15 shows a qualitative comparison of a map generated from one trajectory. It is clear that CFAR does not provide any meaningful features to extract *keypoints* while RadarHD achieves a structurally similar map compared to the lidar. Table. 5 shows the Euclidean distance error between *keypoints* across different environments. Good performance on odometry and

mapping is only possible because of artifact free, structurally meaningful point clouds generated by our network.

7.5 System Efficiency

RadarHD’s entire network uses 17.5 million parameters and takes 12.5 hours to train on our training data on 1 nVidia RTX 3090 GPU. The model size is 210MB in .pt format. We compare inference times on RTX 3090 and an embedded GPU nVidia Jetson Xavier NX. On RTX 3090, each inference takes 5.9 ms (167.5 FPS). On Jetson Xavier NX, inference takes 76.6 ms (13 FPS). This shows promise for running our system on an embedded GPU in real-time.

8 LIMITATIONS

We highlight two key limitations of RadarHD in this work that we hope to remedy in future work: (1) Primarily because of extremely poor elevation resolution (compared to even azimuth) with AWR1843 radar, RadarHD tackles the 2D super resolution problem first rather than 3D. We are confident based on our results that with more data and training that 3D imaging should be possible; (2) RadarHD also only considers static scenes while the car is moving. As we grow our dataset, we are expanding the scope to include handheld radars and dynamic scenes such as people moving. RadarHD shows promise for achieving this when conditioned with the right training data.

9 CONCLUSION

RadarHD creates a lidar-like high resolution point cloud from low resolution single-chip mmWave radar input to obtain high-quality point clouds in scenarios where lidar fails. RadarHD custom designs a machine learning pipeline for this task and overcomes the challenges arising from radar artifacts by carefully choosing machine learning design parameters. We show our rich point cloud on a wide variety of scenes including completely new environments unobserved during training and even in significant occlusions such as smoke. In building this system, we collect a large dataset of radar-lidar raw data pairs, which can potentially be useful for other perception tasks. Perhaps the most important element of this work is the network design methodology that stands as a blueprint for applying learning techniques to other forms of radar processing.

REFERENCES

- [1] 2022. Sorensen-Dice Coefficient. https://en.wikipedia.org/wiki/S%C3%B8rensen%E2%80%93Dice_coefficient.
- [2] Fadel Adib, Chen-Yu Hsu, Hongzi Mao, Dina Katabi, and Frédo Durand. 2015. Capturing the human figure through a wall. *ACM Transactions on Graphics (TOG)* 34, 6 (2015), 1–13.
- [3] Roberto Aldera, Daniele De Martini, Matthew Gadd, and Paul Newman. 2019. Fast radar motion estimation with a learnt focus of attention using weak supervision. In *2019 International Conference on Robotics and Automation (ICRA)*. IEEE, 1190–1196.
- [4] Roberto Aldera, Daniele De Martini, Matthew Gadd, and Paul Newman. 2019. What could go wrong? introspective radar odometry in challenging environments. In *2019 IEEE Intelligent Transportation Systems Conference (ITSC)*. IEEE, 2835–2842.
- [5] Yasin Almalioglu, Mehmet Turan, Chris Xiaoxuan Lu, Niki Trigoni, and Andrew Markham. 2020. Milli-RIO: Ego-motion estimation with low-cost millimetre-wave radar. *IEEE Sensors Journal* 21, 3 (2020), 3314–3323.
- [6] Roger Appleby and Rupert N Anderton. 2007. Millimeter-wave and submillimeter-wave imaging for security and surveillance. *Proc. IEEE* 95, 8 (2007), 1683–1690.
- [7] Kshitiz Bansal, Keshav Rungta, Siyuan Zhu, and Dinesh Bharadia. 2020. Pointillism: Accurate 3d bounding box estimation with multi-radars. In *Proceedings of the 18th Conference on Embedded Networked Sensor Systems*. 340–353.
- [8] John L Barron, Robert E Mercer, X Chen, and Paul Joe. 2005. 3d velocity from 3d doppler radial velocity. *International Journal of Imaging Systems and Technology* 15, 3 (2005), 189–198.
- [9] Andrew Bell, Brad Chambers, and Howard Butler. 2022. Point Data Abstraction Library. <https://pdal.io/apps/chamfer.html>.
- [10] Andrew Bell, Brad Chambers, and Howard Butler. 2022. Point Data Abstraction Library. "<https://pdal.io/apps/hausdorff.html>".
- [11] Jonas Callmer, David Törnqvist, Fredrik Gustafsson, Henrik Svensson, and Pelle Carlbom. 2011. Radar SLAM using visual features. *EURASIP Journal on Advances in Signal Processing* 2011, 1 (2011), 1–11.
- [12] Sarah H Cen and Paul Newman. 2018. Precise ego-motion estimation with millimeter-wave radar under diverse and challenging conditions. In *2018 IEEE International Conference on Robotics and Automation (ICRA)*. IEEE, 6045–6052.
- [13] Alex Kendall Christof Angermueller. 2022. Convolutional Neural Networks. http://cbl.eng.cam.ac.uk/pub/Intranet/MLG/ReadingGroup/cnn_basics.pdf.
- [14] Ruoxi Deng, Chunhua Shen, Shengjun Liu, Huibing Wang, and Xinru Liu. 2018. Learning to predict crisp boundaries. In *Proceedings of the European Conference on Computer Vision (ECCV)*. 562–578.
- [15] Kedar Dhamdhere, Mukund Sundararajan, and Qiqi Yan. 2018. How important is a neuron? *arXiv preprint arXiv:1805.12233* (2018).
- [16] Martin Dimitrievski, Peter Veelaert, and Wilfried Philips. 2017. Semantically aware multilateral filter for depth upsampling in automotive lidar point clouds. In *2017 IEEE Intelligent Vehicles Symposium (IV)*. IEEE, 1058–1063.
- [17] Li Ding and Gaurav Sharma. 2017. Fusing structure from motion and lidar for dense accurate depth map estimation. In *2017 IEEE International Conference on Acoustics, Speech and Signal Processing (ICASSP)*. IEEE, 1283–1287.
- [18] C Doer and GF Trommer. 2021. x-RIO: Radar Inertial Odometry with Multiple Radar Sensors and Yaw Aiding. *Gyroscopy and Navigation* 12, 4 (2021), 329–339.
- [19] Christopher Doer and Gert F Trommer. 2020. An ekf based approach to radar inertial odometry. In *2020 IEEE International Conference on Multisensor Fusion and Integration for Intelligent Systems (MFI)*. IEEE, 152–159.
- [20] Christopher Doer and Gert F Trommer. 2020. Radar inertial odometry with online calibration. In *2020 European Navigation Conference (ENC)*. IEEE, 1–10.
- [21] Mohammad Tayeb Ghasr, Matthew J Horst, Matthew R Dvorsky, and Reza Zoughi. 2016. Wideband microwave camera for real-time 3-D imaging. *IEEE Transactions on Antennas and Propagation* 65, 1 (2016), 258–268.

- [22] Daniel Glasner, Shai Bagon, and Michal Irani. 2009. Super-resolution from a single image. In *2009 IEEE 12th international conference on computer vision*. IEEE, 349–356.
- [23] Ian J Goodfellow, Jonathon Shlens, and Christian Szegedy. 2014. Explaining and harnessing adversarial examples. *arXiv preprint arXiv:1412.6572* (2014).
- [24] Junfeng Guan, Sohrab Madani, Suraj Jog, Saurabh Gupta, and Haitham Hassanieh. 2020. Supplementary Materials for Through Fog High Resolution Imaging Using Millimeter Wave Radar. (2020).
- [25] Junfeng Guan, Sohrab Madani, Suraj Jog, Saurabh Gupta, and Haitham Hassanieh. 2020. Through fog high-resolution imaging using millimeter wave radar. In *Proceedings of the IEEE/CVF Conference on Computer Vision and Pattern Recognition*. 11464–11473.
- [26] Axel-Christian Guei and Moulay Akhloufi. 2018. Deep learning enhancement of infrared face images using generative adversarial networks. *Applied optics* 57, 18 (2018), D98–D107.
- [27] Francesco Guidi, Anna Guerra, and Davide Dardari. 2015. Personal mobile radars with millimeter-wave massive arrays for indoor mapping. *IEEE Transactions on Mobile Computing* 15, 6 (2015), 1471–1484.
- [28] Wolfgang Hess, Damon Kohler, Holger Rapp, and Daniel Andor. 2016. Real-Time Loop Closure in 2D LIDAR SLAM. In *2016 IEEE International Conference on Robotics and Automation (ICRA)*. 1271–1278.
- [29] Yan Huang, Wei Wang, and Liang Wang. 2015. Bidirectional recurrent convolutional networks for multi-frame super-resolution. *Advances in neural information processing systems* 28 (2015).
- [30] Texas Instruments. 2022. AWR1843BOOST. "https://www.ti.com/tool/AWR1843BOOST".
- [31] Cesar Iovescu and Sandeep Rao. 2017. The fundamentals of millimeter wave sensors. *Texas Instruments* (2017), 1–8.
- [32] Dominik Kellner, Michael Barjenbruch, Jens Klappstein, Jürgen Dickmann, and Klaus Dietmayer. 2013. Instantaneous ego-motion estimation using doppler radar. In *16th International IEEE Conference on Intelligent Transportation Systems (ITSC 2013)*. IEEE, 869–874.
- [33] Dominik Kellner, Michael Barjenbruch, Jens Klappstein, Jürgen Dickmann, and Klaus Dietmayer. 2014. Instantaneous ego-motion estimation using multiple Doppler radars. In *2014 IEEE International Conference on Robotics and Automation (ICRA)*. IEEE, 1592–1597.
- [34] Narine Kokhlikyan, Vivek Miglani, Miguel Martin, Edward Wang, Bilal Alsallakh, Jonathan Reynolds, Alexander Melnikov, Natalia Kliushkina, Carlos Araya, Siqi Yan, and Orion Reblitz-Richardson. 2020. CapTum: A unified and generic model interpretability library for PyTorch. *arXiv:2009.07896 [cs.LG]*
- [35] Andrew Kramer, Carl Stahoviak, Angel Santamaria-Navarro, Ali-Akbar Agha-Mohammadi, and Christoffer Heckman. 2020. Radar-inertial ego-velocity estimation for visually degraded environments. In *2020 IEEE International Conference on Robotics and Automation (ICRA)*. IEEE, 5739–5746.
- [36] Christian Ledig, Lucas Theis, Ferenc Huszár, Jose Caballero, Andrew Cunningham, Alejandro Acosta, Andrew Aitken, Alykhan Tejani, Johannes Totz, Zehan Wang, et al. 2017. Photo-realistic single image super-resolution using a generative adversarial network. In *Proceedings of the IEEE conference on computer vision and pattern recognition*. 4681–4690.
- [37] Vladimir Lekic and Zdenka Babic. 2019. Automotive radar and camera fusion using generative adversarial networks. *Computer Vision and Image Understanding* 184 (2019), 1–8.
- [38] Jaime Lien, Nicholas Gillian, M Emre Karagozler, Patrick Amihoud, Carsten Schwesig, Erik Olson, Hakim Raja, and Ivan Poupyrev. 2016. Soli: Ubiquitous gesture sensing with millimeter wave radar. *ACM Transactions on Graphics (TOG)* 35, 4 (2016), 1–19.
- [39] Yunfei Long, Daniel Morris, Xiaoming Liu, Marcos Castro, Punarjay Chakravarty, and Praveen Narayanan. 2021. Full-Velocity Radar Returns by Radar-Camera Fusion. In *Proceedings of the IEEE/CVF International Conference on Computer Vision*. 16198–16207.
- [40] Chris Xiaoxuan Lu, Stefano Rosa, Peijun Zhao, Bing Wang, Changhao Chen, John A Stankovic, Niki Trigoni, and Andrew Markham. 2020. See through smoke: robust indoor mapping with low-cost mmwave radar. In *Proceedings of the 18th International Conference on Mobile Systems, Applications, and Services*. 14–27.
- [41] Chris Xiaoxuan Lu, Stefano Rosa, Peijun Zhao, Bing Wang, Changhao Chen, Niki Trigoni, and Andrew Markham. 2019. millimap: Robust indoor mapping with low-cost mmwave radar. *arXiv preprint arXiv:1911.00398* (2019).
- [42] Chris Xiaoxuan Lu, Muhammad Risqi U Saputra, Peijun Zhao, Yasin Al-malioglu, Pedro PB de Gusmao, Changhao Chen, Ke Sun, Niki Trigoni, and Andrew Markham. 2020. milliEgo: mmWave Aided Egomotion Estimation with Deep Sensor Fusion. *arXiv preprint arXiv:2006.02266* (2020).
- [43] Babak Mamandipoor, Greg Malysa, Amin Arbabian, Upamanyu Madhoo, and Karam Noujeim. 2014. 60 ghz synthetic aperture radar for short-range imaging: Theory and experiments. In *2014 48th Asilomar Conference on Signals, Systems and Computers*. IEEE, 553–558.
- [44] Yang Meng, Anyong Qing, Chuan Lin, Jiefeng Zang, Yizhe Zhao, and Cheng Zhang. 2018. Passive millimeter wave imaging system based on helical scanning. *Scientific reports* 8, 1 (2018), 1–12.
- [45] Mostafa Mostafa, Shady Zahran, Adel Moussa, Naser El-Sheimy, and Abu Sesay. 2018. Radar and visual odometry integrated system aided navigation for UAVS in GNSS denied environment. *Sensors* 18, 9 (2018), 2776.
- [46] David Murdoch. 2021. *Augmentation of Visual Odometry using Radar*. Master's thesis. University of Waterloo.
- [47] Ramin Nabati and Hairong Qi. 2021. Centerfusion: Center-based radar and camera fusion for 3d object detection. In *Proceedings of the IEEE/CVF Winter Conference on Applications of Computer Vision*. 1527–1536.
- [48] Arthur Ouaknine, Alasdair Newson, Julien Rebut, Florence Tupin, and Patrick Perez. 2021. Carrada dataset: Camera and automotive radar with range-angle-doppler annotations. In *2020 25th International Conference on Pattern Recognition (ICPR)*. IEEE, 5068–5075.
- [49] Yeong Sang Park, Young-Sik Shin, Joowan Kim, and Ayoung Kim. 2021. 3D ego-Motion Estimation Using low-Cost mmWave Radars via Radar Velocity Factor for Pose-Graph SLAM. *IEEE Robotics and Automation Letters* 6, 4 (2021), 7691–7698.
- [50] Ioannis Pefkianakis and Kyu-Han Kim. 2018. Accurate 3D localization for 60 GHz networks. In *Proceedings of the 16th ACM Conference on Embedded Networked Sensor Systems*. 120–131.
- [51] Akarsh Prabhakara, Vaibhav Singh, Swarn Kumar, and Anthony Rowe. 2020. Osprey: a mmWave approach to tire wear sensing. In *Proceedings of the 18th International Conference on Mobile Systems, Applications, and Services*. 28–41.
- [52] Cristiano Premebida, Luis Garrote, Alireza Asvadi, A Pedro Ribeiro, and Urbano Nunes. 2016. High-resolution lidar-based depth mapping using bilateral filter. In *2016 IEEE 19th international conference on intelligent transportation systems (ITSC)*. IEEE, 2469–2474.
- [53] Kun Qian, Zhao Yuan He, and Xinyu Zhang. 2020. 3D Point Cloud Generation with Millimeter-Wave Radar. *Proc. ACM Interact. Mob. Wearable Ubiquitous Technol.* 4, 4, Article 148 (dec 2020), 23 pages. <https://doi.org/10.1145/3432221>
- [54] Eric B Quist and Randal W Beard. 2016. Radar odometry on fixed-wing small unmanned aircraft. *IEEE Trans. Aerospace Electron. Systems* 52, 1 (2016), 396–410.
- [55] Matthias Rapp, Michael Barjenbruch, Klaus Dietmayer, Markus Hahn, and Jürgen Dickmann. 2015. A fast probabilistic ego-motion estimation framework for radar. In *2015 European Conference on Mobile Robots*

- (ECMR). IEEE, 1–6.
- [56] Mark A Richards. 2005. *Fundamentals of radar signal processing*. Tata McGraw-Hill Education.
 - [57] Olaf Ronneberger, Philipp Fischer, and Thomas Brox. 2015. U-net: Convolutional networks for biomedical image segmentation. In *International Conference on Medical image computing and computer-assisted intervention*. Springer, 234–241.
 - [58] Timofey Savelyev, Xiaodong Zhuge, Bill Yang, Alexander Yarovsky, Leo Ligthart, Michail Drozdov, and Boris Levitas. 2010. Development of UWB microwave array radar for concealed weapon detection. In *11-th INTERNATIONAL RADAR SYMPOSIUM*. IEEE, 1–4.
 - [59] AF Scannapieco, A Renga, G Fasano, and A Moccia. 2017. Ultralight radar for small and micro-uav navigation. *The International Archives of Photogrammetry, Remote Sensing and Spatial Information Sciences* 42 (2017), 333.
 - [60] Antonio Fulvio Scannapieco, Alfredo Renga, Giancarmine Fasano, and Antonio Moccia. 2018. Experimental analysis of radar odometry by commercial ultralight radar sensor for miniaturized UAS. *Journal of Intelligent & Robotic Systems* 90, 3 (2018), 485–503.
 - [61] Frank Schuster, Christoph Gustav Keller, Matthias Rapp, Martin Hauéis, and Cristóbal Curio. 2016. Landmark based radar SLAM using graph optimization. In *2016 IEEE 19th International Conference on Intelligent Transportation Systems (ITSC)*. IEEE, 2559–2564.
 - [62] Frank Schuster, Marcus Wörner, Christoph Gustav Keller, Martin Hauéis, and Cristóbal Curio. 2016. Robust localization based on radar signal clustering. In *2016 IEEE Intelligent Vehicles Symposium (IV)*. IEEE, 839–844.
 - [63] David M Sheen, Douglas L McMakin, and Thomas E Hall. 2007. Near field imaging at microwave and millimeter wave frequencies. In *2007 IEEE/MTT-S International Microwave Symposium*. IEEE, 1693–1696.
 - [64] Avanti Shrikumar, Jocelin Su, and Anshul Kundaje. 2018. Computationally efficient measures of internal neuron importance. *arXiv preprint arXiv:1807.09946* (2018).
 - [65] Karen Simonyan, Andrea Vedaldi, and Andrew Zisserman. 2013. Deep inside convolutional networks: Visualising image classification models and saliency maps. *arXiv preprint arXiv:1312.6034* (2013).
 - [66] Akash Deep Singh, Sandeep Singh Sandha, Luis Garcia, and Mani Srivastava. 2019. Radhar: Human activity recognition from point clouds generated through a millimeter-wave radar. In *Proceedings of the 3rd ACM Workshop on Millimeter-wave Networks and Sensing Systems*. 51–56.
 - [67] PR Smith. 1981. Bilinear interpolation of digital images. *Ultramicroscopy* 6, 2 (1981), 201–204.
 - [68] Joseph W Starr and BY Lattimer. 2014. Evaluation of navigation sensors in fire smoke environments. *Fire Technology* 50, 6 (2014), 1459–1481.
 - [69] Damien Vivet, Paul Checchin, and Roland Chapuis. 2013. Localization and mapping using only a rotating FMCW radar sensor. *Sensors* 13, 4 (2013), 4527–4552.
 - [70] Xintao Wang, Ke Yu, Shixiang Wu, Jinjin Gu, Yihao Liu, Chao Dong, Yu Qiao, and Chen Change Loy. 2018. Esrgan: Enhanced super-resolution generative adversarial networks. In *Proceedings of the European conference on computer vision (ECCV) workshops*. 0–0.
 - [71] Claire M Watts, Patrick Lancaster, Andreas Pedross-Engel, Joshua R Smith, and Matthew S Reynolds. 2016. 2D and 3D millimeter-wave synthetic aperture radar imaging on a PR2 platform. In *2016 IEEE/RSJ International Conference on Intelligent Robots and Systems (IROS)*. IEEE, 4304–4310.
 - [72] Teng Wei and Xinyu Zhang. 2015. mtrack: High-precision passive tracking using millimeter wave radios. In *Proceedings of the 21st Annual International Conference on Mobile Computing and Networking*. 117–129.
 - [73] Chenshu Wu, Feng Zhang, Beibei Wang, and KJ Ray Liu. 2020. mm-Track: Passive multi-person localization using commodity millimeter wave radio. In *IEEE INFOCOM 2020-IEEE Conference on Computer Communications*. IEEE, 2400–2409.
 - [74] Tong Wu, Liang Pan, Junzhe Zhang, Tai Wang, Ziwei Liu, and Dahua Lin. 2021. Density-aware chamfer distance as a comprehensive metric for point cloud completion. *arXiv preprint arXiv:2111.12702* (2021).
 - [75] Jingao Xu, Guoxuan Chi, Zheng Yang, Danyang Li, Qian Zhang, Qiang Ma, and Xin Miao. 2021. FollowUpAR: enabling follow-up effects in mobile AR applications. In *Proceedings of the 19th Annual International Conference on Mobile Systems, Applications, and Services*. 1–13.
 - [76] Hiroyoshi Yamada, Takumi Kobayashi, Yoshio Yamaguchi, and Yuuichi Sugiyama. 2017. High-resolution 2D SAR imaging by the millimeter-wave automobile radar. In *2017 IEEE Conference on Antenna Measurements & Applications (CAMA)*. IEEE, 149–150.
 - [77] Muhammet Emin Yanik and Murat Torlak. 2019. Near-field MIMO-SAR millimeter-wave imaging with sparsely sampled aperture data. *Ieee Access* 7 (2019), 31801–31819.
 - [78] Jason Yosinski, Jeff Clune, Anh Nguyen, Thomas Fuchs, and Hod Lipson. 2015. Understanding neural networks through deep visualization. *arXiv preprint arXiv:1506.06579* (2015).
 - [79] Mingmin Zhao, Tianhong Li, Mohammad Abu Alsheikh, Yonglong Tian, Hang Zhao, Antonio Torralba, and Dina Katabi. 2018. Through-wall human pose estimation using radio signals. In *Proceedings of the IEEE Conference on Computer Vision and Pattern Recognition*. 7356–7365.
 - [80] Mingmin Zhao, Yonglong Tian, Hang Zhao, Mohammad Abu Alsheikh, Tianhong Li, Rumen Hristov, Zachary Kabelac, Dina Katabi, and Antonio Torralba. 2018. RF-based 3D skeletons. In *Proceedings of the 2018 Conference of the ACM Special Interest Group on Data Communication*. 267–281.
 - [81] Peijun Zhao, Chris Xiaoxuan Lu, Bing Wang, Niki Trigoni, and Andrew Markham. 2021. 3D Motion Capture of an Unmodified Drone with Single-chip Millimeter Wave Radar. In *2021 IEEE International Conference on Robotics and Automation (ICRA)*. IEEE, 5186–5192.
 - [82] Anfu Zhou, Shaoyuan Yang, Yi Yang, Yuhang Fan, and Huadong Ma. 2019. Autonomous environment mapping using commodity millimeter-wave network device. In *IEEE INFOCOM 2019-IEEE Conference on Computer Communications*. IEEE, 1126–1134.